



a phase growth and branching in titanium alloys

Rongpei Shi^a, Deep Choudhuri ¹

b*, Ankush Kashiwar^{c†}, Sriswaroop Dasari^b, Yunzhi Wang ¹

d, Rajarshi Banerjee and Dipankar Banerjee ¹

^aMaterials Science Division, Lawrence Livermore National Laboratory, Livermore, CA, USA;
^bDepartment of Materials Science and Engineering, University of North Texas, Denton, TX, USA;
^cDepartment of Materials Engineering, Indian Institute of Science, Bangalore, India;
^dDepartment of Materials Science and Engineering, Ohio State University, Columbus, OH, USA

ABSTRACT

The morphology and spatial distribution of alpha (g) precipitates have been mapped as a function of Mo content in Ti-Mo binary alloys employing a combinatorial approach. Heat-treatments were carried out compositionally graded Ti-xMo samples processed using a rapid throughput laser engineered net shape (LENS) process. The composition space spans 1.5 at% to 6 at% Mo with ageing at 750°C, 650°C and 600°C following a β solution treatment. Three distinct regimes of a morphology and distribution were observed. These are colonydominated microstructures originating from grain boundary a allotriomorphs, bundles of intragranular a laths, and homogeneously distributed individual fine-scale a laths. Branching of the a precipitates was observed in all these domains in a manner reminiscent of solid-state dendritic growth. The phenomenon is particularly apparent at low volume fractions of a. Similar features are present in a wide variety of alloy compositions. 3-dimensional features of such branched structures have been analysed. Simulation of the branching process by phase field methods incorporating anisotropy in the α/β interface energy and elasticity suggests that it can be initiated at growth ledges present at broad faces of the a laths, driven by the enhancement of the diffusion flux at these steps. The dependence of branching on various parameters such as supersaturation and diffusivity, and microstructural features like ledge height and distribution and the presence of adjacent a variants has been evaluated.

ARTICLE HISTORY

Received 22 November 2020 Accepted 5 October 2021

KEYWORDS

Phase field modelling; 3d metallography; solid state branching

CONTACT Dipankar Banerjee dbanerjee@iisc.ac.in Department of Materials Engineering, Indian Institute of Science, Bangalore 560012, India

^{*}Presently at the Department of Materials and Metallurgical Engineering, New Mexico Institute of Mining and Technology, Socorro, 87801, USA.

¹Presently at EMAT, University of Antwerp, Groenenborgerlaan 171, B-2020 Antwerp, Belgium. Supplemental data for this article can be accessed https://doi.org/10.1080/14786435.2021.1998693

1. Introduction

The properties of titanium alloys derive from its allotropic modification from the high temperature, body centred cubic phase (β, space group Im3m) to the low temperature hexagonal close packed phase (a, space group P63/ mmc). The transformation results in a wide range of spatial distribution, morphology, and scale of α depending upon alloy composition and transformation paths and has been extensively investigated in the past [1,2]. The transformation near the \beta transus is of relevance in alloys with lower beta stabiliser contents (near α and $\alpha+\beta$ alloys) where the low temperature transformation regime cannot be accessed because of rapid transformation kinetics. In contrast, enriched \(\beta \) alloys employ lower ageing temperatures to obtain fine distributions of α phase since the metastable β phase can be retained to room temperature by quenching. In this class of alloys, the influence of precursor phases such as ω on α phase distribution has been investigated in detail recently [3]. The kinetics of the β to α transformation in the Ti-Mo system was established as early as 1952 [4], and microstructures as a function of composition have been examined [5]. We have recently employed [6] a combinatorial approach based on compositionally graded Ti-xMo alloys fabricated by LENS deposition to revisit morphology and distribution of the a phase in a broad domain of temperature and composition space in this system. This study extends earlier work to a detailed analysis of the morphology, spatial distribution, and crystallography of α phase formed in the high temperature ageing domain in which the β to a transformation occurs without intermediate transition phases. In doing so, we find significant a precipitate branching during growth over a large

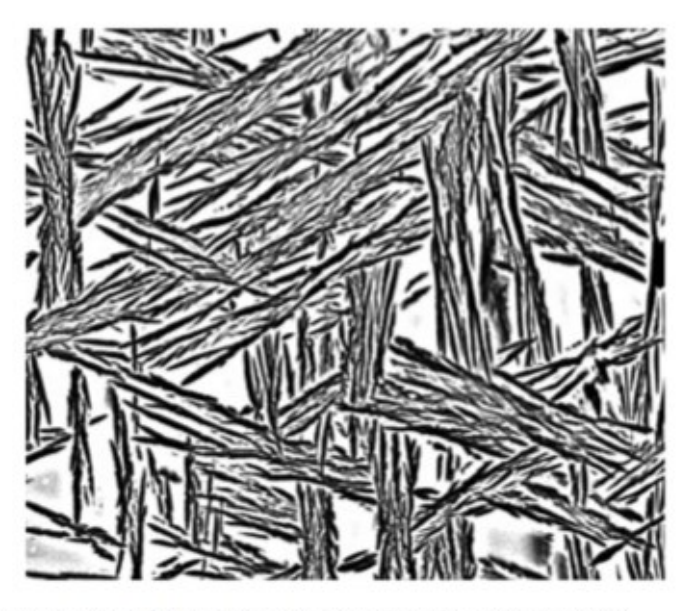


Figure 1. Microstructure of α in a Ti-5.5 at %Mo alloy after aging at 700°C.

temperature and composition space and show the effect of this branching on a distribution that evolves. Figure 1 is illustrative of the phenomenon. Examples of such branched structures exist in [7] and subsequently in numerous other publications too extensive to list. However, their origin had not been examined till Menon and Aaronson [8] attributed the branching to a sympathetic nucleation process. We instead interpret these unusual microstructural features associated with the high temperature transformation domain in terms of a process akin to solid state dendrite formation, simulated using the phase field method. We also include some results on more complex alloys to illustrate the generality of these results.

2. Experimental and modelling procedures

2.1. Experimental details

Microstructure in composition and temperature space was studied on a compositionally graded specimen, heat-treated at different temperatures, LENS* (from Optomec*) was used to deposit a cylindrical specimen on a Ti-6Al-4V plate. Two hoppers (attached on the side of a LENS chamber) containing fine scale Ti and Mo powders were used during the process. The flow rates from each powder feed were varied appropriately to achieve a compositional gradient along the length of the cylindrical deposit (Figure 2a). The deposition was carried out in a chamber purged with argon to minimise oxygen contamination. The composition profile along the length of the deposited specimen varied from ~1.5 at.%Mo (~3 wt.% Mo) to about ~6 at.% Mo (12 wt. %) . All compositions are referred to in at.%. Figure 2b indicates this composition domain in relation to the Ti-Mo phase diagram [2].

The composition associated with a given area of the built up sample was determined by EDX analysis of the scanned area that was large enough to average the composition of the a and \beta phases in the area. The evaluation of

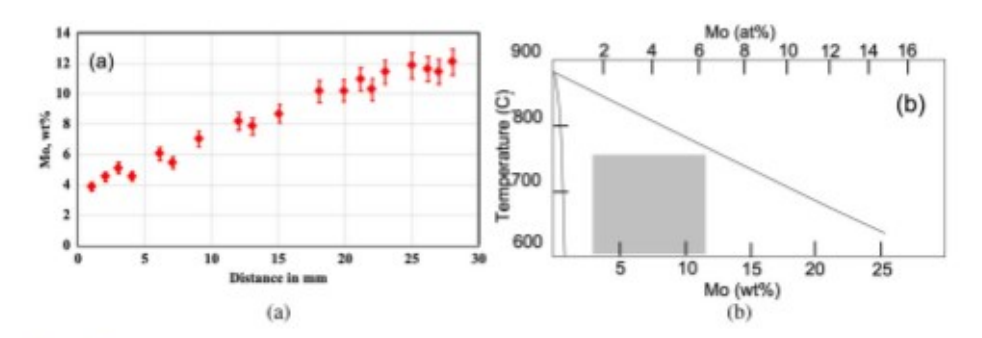


Figure 2. (a) The variation of Mo concentration along the length of the additively built cylinder (b) The Ti-Mo phase diagram [2] with the composition and temperature range examined superimposed on the diagram.

the composition was carried out with background and ZAF correction [9] incorporated using propriety software TEAMTM from EDAX/AMETEK. These correction methods gave an accurate estimate of the composition in a bulk sample of known composition of a Ti-Mo alloy. The error in composition is estimated to be about 7% of the values and is shown in Figure 2. The oxygen content of the LENS samples typically ranged from 0.1–0.2 at.%.

The compositionally graded specimen was β-solutionized (at 1000°C / 30mins) and, subsequently, step quenched to three different temperatures (600, 650 and 750°C) and held there for 30mins, followed by water quenching (WQ). The transformation at 750°C is described in detail in this study, and microstructures at lower temperatures are shown primarily to distinguish between high temperature and lower temperature transformations. These microstructures were evaluated by both backscattered electron (BSE) and electron backscattered diffraction (EBSD) in an FEI Nova 230 NanoSEM scanning electron microscope (SEM) coupled with Hikari Super Electron Backscattered Diffraction (EBSD) detector. EBSD maps were collected at a working distance of ~10 mm after tilting the sample to ~70°. A beam voltage of 20 kV, a current of 6.1 nA and a step size of 40 nm was used to record the maps. The EBSD data analysis was carried out using TSL OIMTM software. A grain boundary distribution map with a minimum misorientation of 1° was used to identify subgrain boundaries, and a Kernel average misorientation was also examined for a branched a group.

In specific cases, transmission electron microscopy (an FEI Tecnai operating at 200 keV) analysis of bulk samples of equivalent compositions was carried out. The 3 mm TEM foils were prepared with conventional techniques: dimple grinding and ion milling at 4 kV. Three-dimensional (3D) images of the α variants were obtained by serial sectioning techniques and reconstruction using proprietary Amira software. Greater detail of these methods is provided in [10]. The microstructures of several other bulk alloy compositions were also examined under similar heat-treatment conditions to compare with the Ti-Mo model system.

2.2. A phase field model for a lath branching

A 3-dimensional phase field model was used to elucidate the physical mechanism underlying the branching phenomena. The morphology development of a single variant of α was initiated by a shape perturbation. The perturbation introduced in the phase field model to stimulate branching is based on the idea that steps or growth ledges are always present on the habit plane of α laths (to accomplish thickening of these laths). These are subject to an enhanced driving force for growth from the diffusion field at these protuberances. Figure 3a shows an example of such growth ledges on the broad face of an α plate, and Figure 3b from the present study shows these ledges in cross-

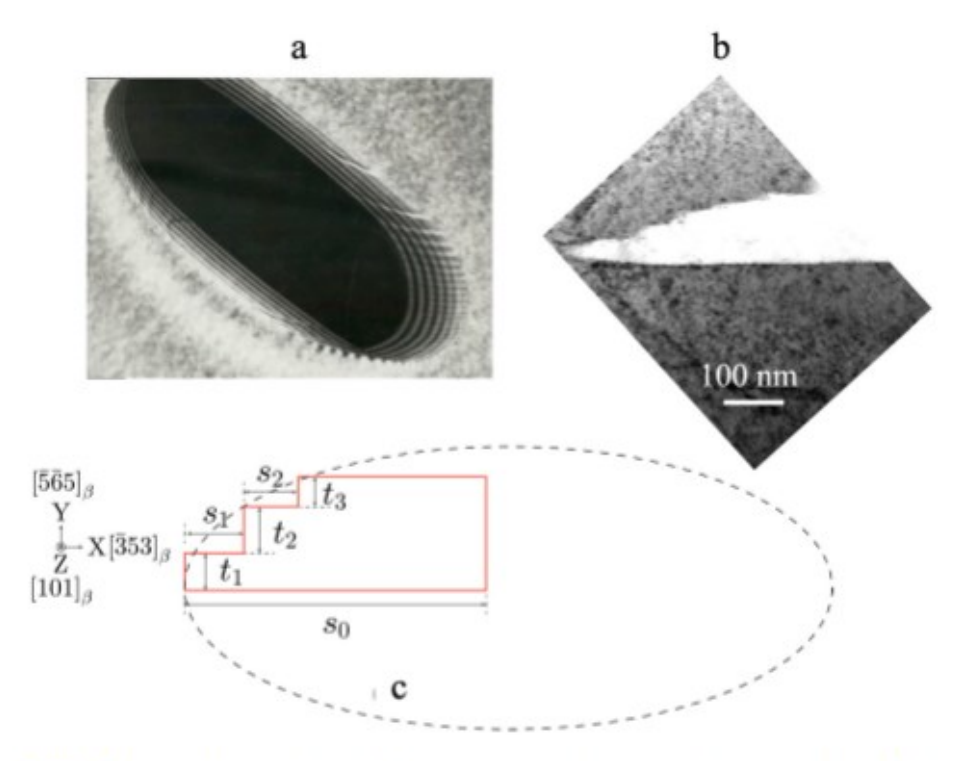


Figure 3. (a) Growth ledges on an α precipitate (reproduced with permission from [1]) (b) growth ledges in cross section at the tip of a α plate with the habit plane edge on (c) the starting configuration of an α lath in the phase field model with steps. t_1 , t_2 and t_3 denote the heights of the ledges. s_1 and s_2 denote the spacing between the ledges. s_0 denotes the length of the α lath. The phase field model simulates a segment of the whole lath towards the tip.

section near the tip of a plate with α appropriately oriented. The growth ledges considered in the current study are of macroscopic height (i.e. much larger than the interatomic distance). Single or multiple steps are introduced in the habit plane in this simulation with the same or different heights. Figure 3c shows a schematic 2D XY cross-section (i.e. the $(101)_{\beta}$ plane) of the starting configuration of an α lath with such steps. s_0 denotes the length of the α lath considered in the simulation. This starting configuration approximates the shape at the tip of an α lath that was experimentally imaged in Figure 3b and does not represent an equilibrium shape. Its purpose is to examine whether the growth ledges that are present can lead to instabilities in growth.

The model incorporates the thermodynamic and kinetic databases available for the well-known Ti6Al4V alloy (Ti-10.2 at%Al-3.6 at%V) as representative of $\alpha+\beta$ alloys in general. Both Gibbs free energy and atomic mobility of each element for the β phase matrix and α phase precipitate are described as a function of alloy composition and temperature in [11]. The methodology adopted to obtain the diffusivity matrix is provided in the supplementary section.

Both solute concentration and crystal structure change across the interface of a single α variant. In the phase field approach, two sets of time and space-dependent order parameters, concentration fields (conserved) $\{X_i(r)\}_{i=Al,V}$ for chemical nonuniformity (Al and V) and a structure order parameter field (nonconserved) $\phi(r)$, change continuously across the interface of a single α variant.

The total free energy of the system consists of the chemical free energy, the surface energy and elastic strain energy and can be formulated as a functional of the order parameters introduced above. The phase field model associated with the branching process has been deployed in our previous studies [12-15]. Therefore, we omit here details of the model framework and formulation of the chemical free energy, elastic strain energy, interfacial energy and its anisotropy, and governing kinetic equations, which can be found in [12-14]. An anisotropic interfacial energy is used in the phase field model. This leads to a variable interface width that is linearly proportional to the interfacial energy for different interface orientations. We have not considered the effect of ledge heights less than 2lo (where lo is the grid size, see Table 1), that is the interface width for the habit plane (broad face). We also point out that our previous phase field simulation studies of α precipitation and variant selection did not incorporate growth ledges on the broad faces of a laths, and thus no branching was observed. The elastic strain energy is a volumetric integral of strain energy density over the whole system derived from microelasticity theory and calculates the elastic strain in the system that exists in both matrix and precipitate phases and is location dependent [12]. The elastic strain field of the precipitate employed is that of a semicoherent precipitate, as is usually observed [16-19]. Therefore, the contribution of the elastic strain to the overall energetics of the process is significantly reduced compared to that of a fully coherent precipitate.

The Burgers orientation relationship for the selected a variant is:

$$(101)_{\beta} \parallel (0001)_{\alpha}, [\bar{1}11]_{\beta} \parallel [11\bar{2}0]_{\alpha}, [\bar{1}\bar{2}1]_{\beta} \parallel [1\bar{1}00]_{\alpha}$$

Table 1. Model parameters and material properties used in the phase field simulations.

Physical properties	Symbol	Value	Unit K	
Temperature	T	1123, 1073, 1023		
Grid size	10	12.5	nm	
Interface width	$2l_0 - 5l_0$	25 - 62.5	nm	
Interfacial energy Broad, Side, End-facet	σ	150, 230, 300	mJ/m ²	
Gradient Coefficients	k_{z_0}	0.15198	J · µm ² /mol	
Hump height	60	192	J/mole	
Interface mobility	Lo	6.0×10^{-8}	$J/m^3/s$	
Molar volume	V _m	10-5	m3/mol	
Elastic constants of B phase	C11, C12, C44	97.7, 82.7, 37.5	GPa	
Lattice parameter of β and α phase	a_B , a_a , c_a	3.196, 2.943, 4.680	Å	
Stress-Free Transformation Strain (SFTS)	$\epsilon_{ij}(i, j = 13)$	-0.049 -0.0031 0 -0.0031 0.067 0 0 0 -0.0003	-	

Table 2. The diffusivity matrix for Al and V in the β phase for different alloy compositions and temperatures.

		Ti-10.2 at%Al-3.6 at% (Ti6Al4V)						Ti-9.64Al-5.79V	
92	(800°C)			(750°C)		(850°C)	(800°C)		
$D_{kj}^{n}(m^2/s) = \begin{bmatrix} D_{AlAl}^{T_1} \\ D_{IMI}^{T_2} \end{bmatrix}$	$\begin{bmatrix} D_{AIV}^{Ti} \\ D_{VV}^{Ti} \end{bmatrix}$	[4.54 0.21	$\begin{bmatrix} 0.29 \\ 8.60 \end{bmatrix} \times 10^{-15}$	2.30 0.11	0.15 4.19 \ \text{\] \times 10^{-15}	8.48 0.33	0.48 16.9 × 10 ⁻¹⁵	2.75	$\begin{bmatrix} 0.78 \\ 2.39 \end{bmatrix} \times 10^{-15}$

Three non-coplanar vectors were chosen as the axes of the reference coordinate, i.e. $X \parallel [\bar{3}53]_B$, $Y \parallel [\bar{5}\bar{6}5]_B$ and $Z \parallel [101]_B$. The selection of such a reference coordinate takes into account that the growth direction and habit plane normal of the α lath are aligned along $[\bar{3}53]_{\beta}$ and $[\bar{5}\bar{6}5]_{\beta}$, respectively. We note that there are slightly different descriptions of the habit plane and the invariant line direction or growth direction [16-19].

All simulations were performed using simulation size $320\Delta x \times 32\Delta y \times 128\Delta z$ with equal spatial step size along the x, y and z directions, where $\Delta x = \Delta y = \Delta z = l_0 = 12.5$ nm. Periodical boundary conditions are used along all three dimensions. The ratio between the interfacial energies of the broad, side and end faces of an α lath is 1:2:3, with the energy of the end face as 300 mJm⁻². An α precipitate with its equilibrium composition was placed at the centre of the simulation box filled with B matrix with the alloy composition. All model parameters and physical properties are documented in Table 1 and Table 2. The simulation of a growth effects was carried out at 850°C, 800°C and 750°C for the alloy, which has aα/β transus of 942°C. In addition, a slightly different alloy composition was used in one case to examine the effect of supersaturation alone.

3. Results

3.1. The morphology, spatial distribution, and crystallography of the α phase

Figure 4 shows the variation in α distribution and morphology (within prior β grains) as a function of Mo content on step quenching to 750°C. The BSE images show both grain boundary and intragranular areas. The microstructure at lower Mo concentrations is dominated by α colonies of parallel laths emanating as sideplates from the nearly continuous grain boundary a film. As is well known [1], these sideplates that form the colony have the same crystallographic orientation as the grain boundary a film from which they grow. With increasing Mo concentration, interweaving bundles of α laths form within the grains. The size of these intragranular bundles progressively decreases with increasing Mo content. Figure 5 shows the nature of the colony a emanating from grain boundaries and intragranular α at higher magnification. Figure 5a from a region corresponding to Ti-1.5Mo shows that each α sideplate (in dark contrast) in the colony structure appears to fork extensively. Figure 5b from an

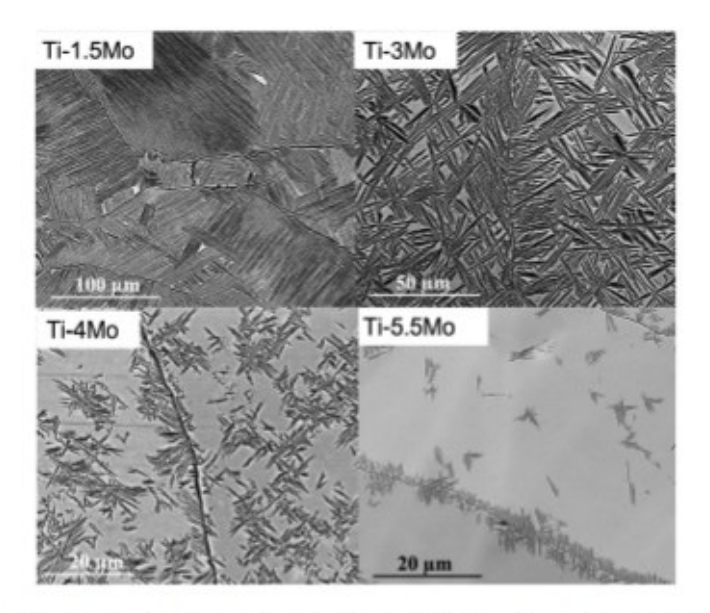


Figure 4. Microstructure of α as a function of Mo concentration on aging at 750°C.

area corresponding to Ti-3Mo suggests that the intragranular bundles are composed of α lath segments oriented roughly parallel to each other. There is a significant increase in the volume fraction of the α phase when the Ti-3Mo composition is aged at 600°C (Figure 5c). The α phase appears as individual laths rather than as bundles. However, forking at the tips of the laths and branching from its broad faces is still evident, as shown by the arrow.

A comparison of the microstructures for different Mo contents in Figure 4 suggests that the intragranular a structure observed in Ti-3Mo originates from the structures observed in Ti-4Mo and Ti-5.5Mo that capture the increasingly early stages of the transformation. Therefore, while all the Ti-xMo compositions in the graded alloy have been isothermally annealed for the same time, the changes in microstructure with increasing Mo content indicate an inverse time scale in evolution. Figure 6 captures the evolution of structure described above through 3d metallography combined with EBSD. The early stage of the formation of such bundles is shown from a Ti5553 alloy (a) commercial designation corresponding to Ti-5Al-5V-5Mo-3Cr-O.35Fe in wt% (Ti-8.8Al-4.7%V-2.5%Mo-2.7%Cr-0.3%Fe in at%) with a β-transus of 865°C. The alloy was step quenched from above the β transus to 700°C and held for 1 h. The microstructure is similar to that of the Ti-5.5Mo, shown in Figure 4. Individual α laths fork and develop perturbations on their surface (Figure 6a). As the 3D image makes clear, extensive forking or branching of a laths leads to an apparent appearance, in 2D sections, of several discrete a laths that are actually branches from a single lath (leading to the description of these as bundles earlier in the paper). The EBSD OIM images in Figure 6 show that these 'bundles' arise from multiply branched a laths that belong to the same crystallographic variant. Trivariant

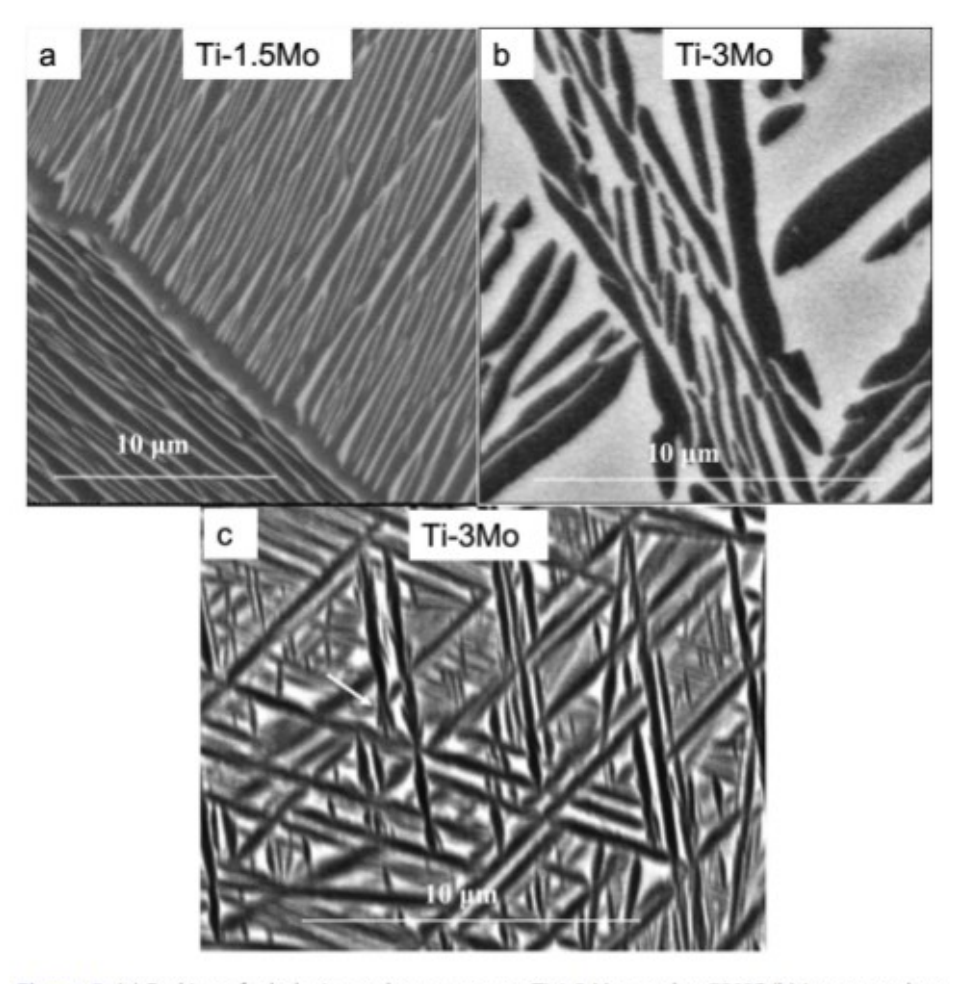


Figure 5: (a) Forking of α laths in a colony structure, Ti-1.5 Mo aged at 750°C (b) intragranular α bundles, Ti-3Mo aged at 750°C (c) The Ti-3Mo aged at 600°C. The α phase is in dark contrast in all these images.

clusters of such bundles are commonly observed (encircled in the BSE image of Figure 6b and c) and possess unique crystallography in that the 3 variants in a cluster have a common [1120] axis parallel to a specific [111] of the parent β grain. This feature has been analysed in earlier work [20,21].

Figure 7 is a detailed analysis through high resolution EBSD of the misorientations that may be present within such an individual bundle in two ways. First, Figure 7b shows an analysis of subgrain boundaries in the same bundle and shows that boundaries between 1° and 5° are not present even at locations where different parallel branches join. Another way of examining misorientations within a bundle is to analyse the kernel average misorientation (KAM), as shown in Figure 7c. The average spread in misorientations is about 0.5°, and the outliers of 1.5°-2° are located at the α/β interface and might arise from interface strain.

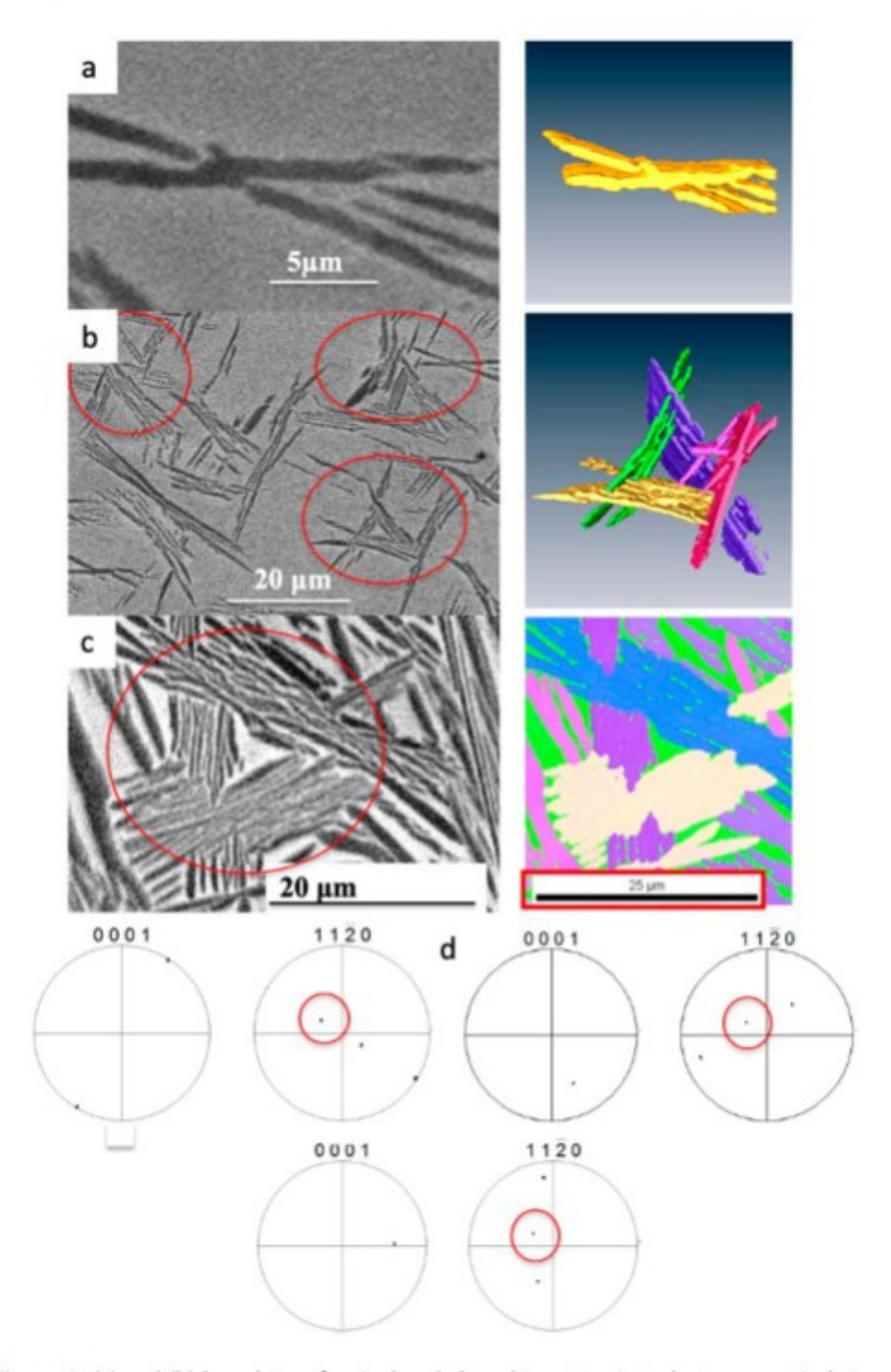


Figure 6. (a) and (b) branching of a single α lath and in a trivariant cluster respectively in a Ti5553 alloy step quenched from above the β transus to 700°C and held for 1 h (c) evolution of branched structures to trivariant bundles of α laths in Ti-3Mo aged at 750°C (d) typical pole figures from areas such as in (b) and (c) showing that α variants in the trivariant cluster have a common [11 $\bar{2}$ 0] direction.

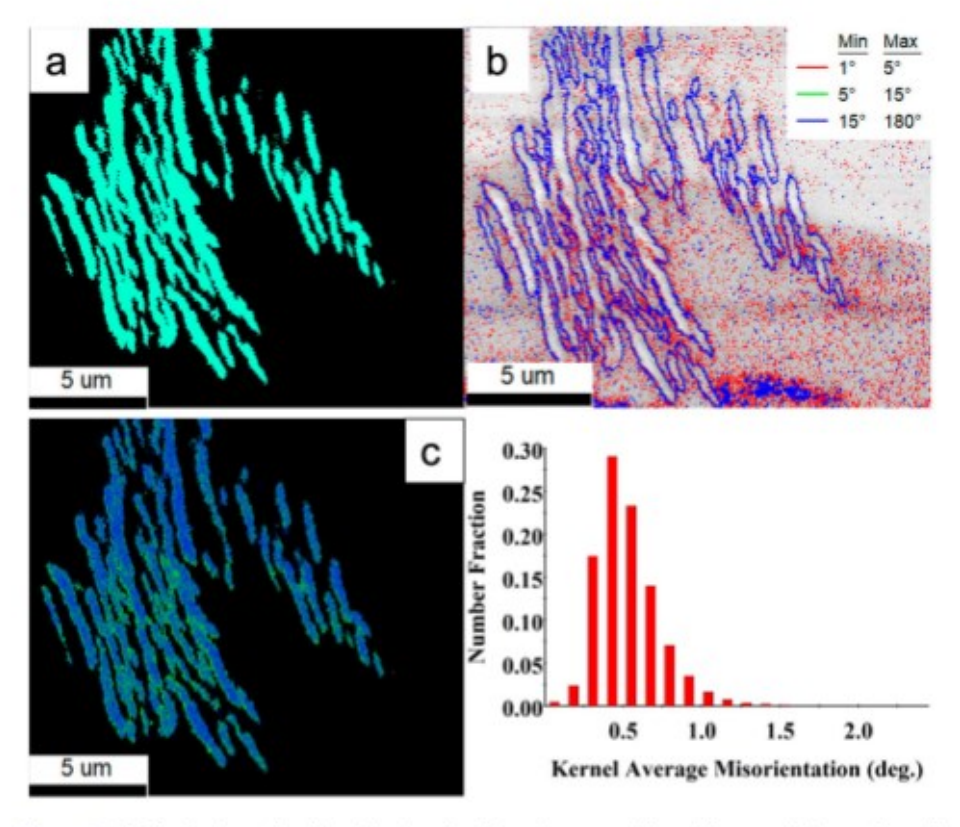


Figure 7. EBSD of a branched bundle showing (a) a phase partitioned image of the α phase (b) a grain boundary misorientation map showing that no subgrain boundaries are seen within the bundles with misorienations between 1° and 5° and the only boundaries observed are the α/β interfaces (c) the kernel average misorientation map (KAM) showing the distribution of misorientations.

Transmission electron microscopy of such a bundle is shown in Figure 8. The α laths exhibit the Burgers orientation relationship with the β matrix:

$$(101)_{\beta} \parallel (0001)_{\alpha}, [\bar{1}11]_{\beta} \parallel [11\bar{2}0]_{\alpha}, (12\bar{1})_{\beta} \parallel (1\bar{1}00)_{\alpha}$$

The morphology of individual α laths can be approximated [16] to a rectangular slab with a broad face of low surface energy with a habit plane that deviates by about 14° from $(12\bar{1})_{\beta} \parallel (1\bar{1}00)_{\alpha}$, a side face of intermediate surface energy that is closely parallel to $(0001)_{\alpha}$ // $(101)_{\beta}$, and a largely incoherent end facet that lies perpendicular to the growth direction which deviates marginally from $[11\bar{2}0]_{\alpha}$ // $[\bar{1}11]_{\beta}$. Figure 8a along the [0001] α direction parallel to $[110]_{\beta}$ shows the branching of a single α lath from its point of origin. The habit planes of these branches and their growth directions are not identical but scatter about a mean. Figures 8 b and c show images in mutually perpendicular orientations to Figure 8a. The broad face of the laths is roughly parallel to $(12\bar{1})_{\beta} \parallel (1\bar{1}00)_{\alpha}$ and is seen in Figure 8c.



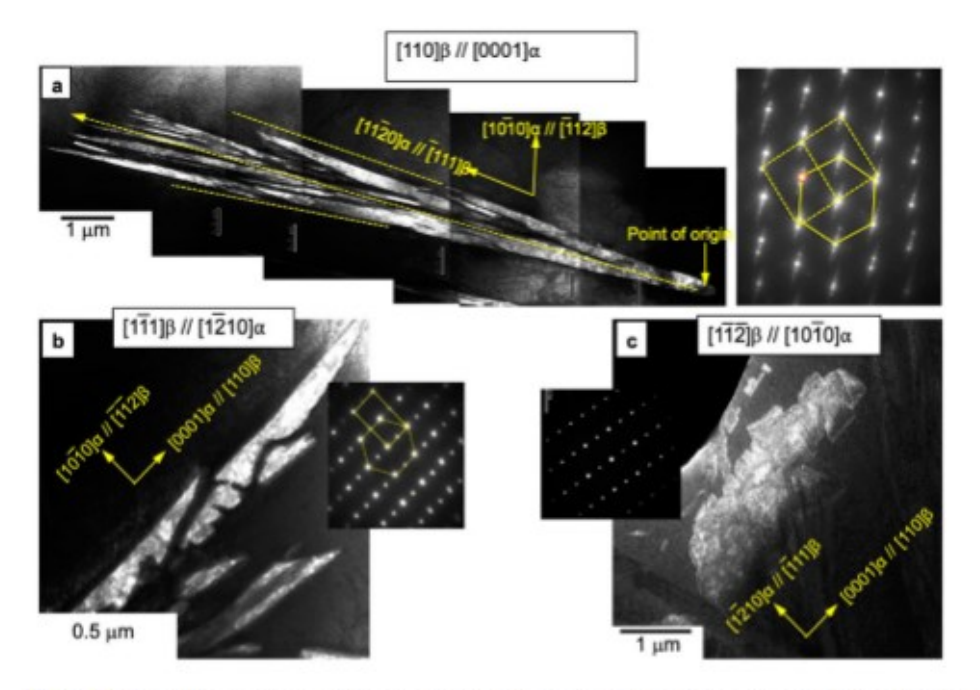


Figure 8. Transmission electron microscopy of multiply branched α laths imaged in 3 mutually perpendicular orientations. The zone axes are indicated on the respective figures. The α and β pattern overlap completely in (c). The expected habit plane is indicted in (a) by the yellow dashed line with an arrow.

We have examined other alloys to see if branching as described above is reproduced in different compositions. Since Al is a critical alloying element added in most commercial Ti alloys, and the Ti-V-Al and Ti-Mo-Al systems form the basis of many commercial Ti alloys such as Ti-64, Ti-5553 and Beta-21S, four different alloys with the compositions Ti-3Mo-5Al, Ti-5Mo-5Al, Ti-1.5V and Ti-9V-9Al (all in at%) were arc melted and subsequently solution treated, step quenched to 750°C and isothermally held for 30mins. Microstructures of these four alloys, shown in Figure 9, invariably consisted of bundles of multiply branched or forked α laths.

3.2. Phase field modelling of a lath branching

The experimental results described in the previous section indicate that ageing at high temperatures results in the formation of α laths that show significant branching reminiscent of a solid-state dendritic structure. We have assumed in the phase field simulation that the presence of sharp corners arising at the risers of growth ledges at the tips of α laths, as shown in Figure 3, may provide a source for the branching, i.e. the steps provide a pre-existing perturbation in the structure that can originate an instability. We first employed the phase field simulation to examine the development of branching in a single α

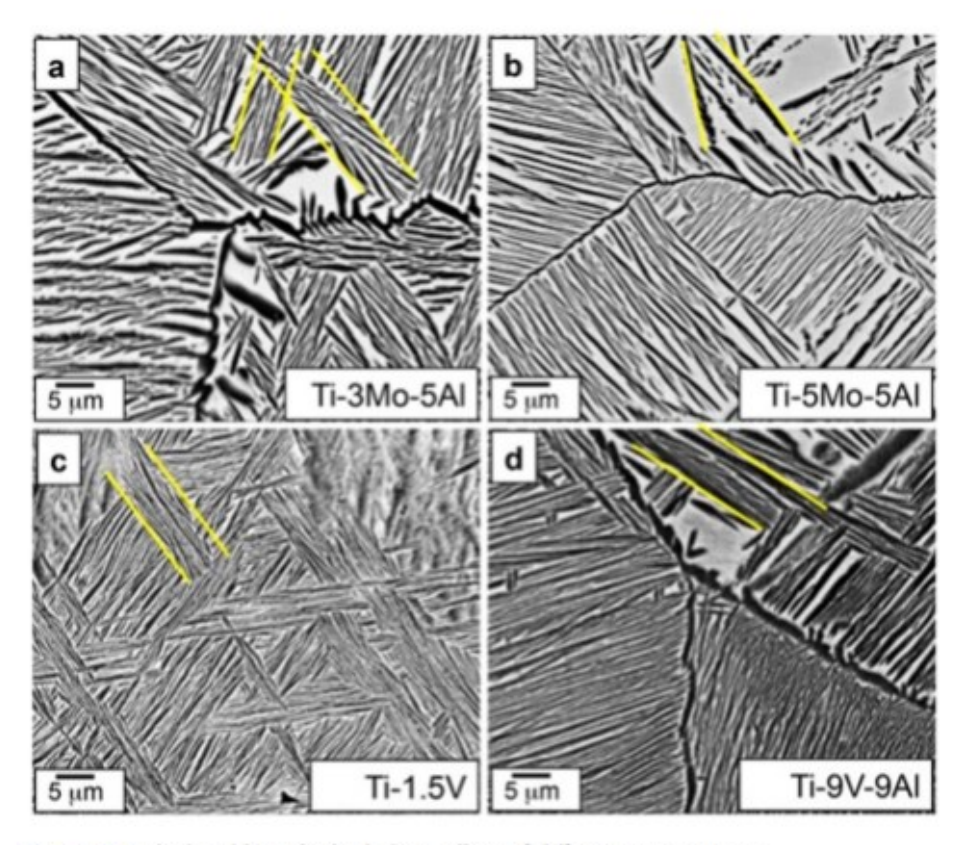


Figure 9. Forked and branched α laths in alloys of different compositions.

lath with varying starting ledge (step) heights and thickness for a single ledge. The results are shown in Figure 10. It is seen in Figure 10a that the sharp corner due to the presence of a growth ledge near the tip grows out faster than the flat interface. A comparison of Figure 10a with 10b indicates that a lower growth ledge height (t2), keeping the base lath thickness (t1) a constant, delays the onset of the branching. This suggests that a critical ledge height may be required for branching to initiate. The starting lath thickness has been reduced in Figure 10c and suggests that finer α laths may delay branching. Figure 10d shows a 3d view of the section of Figure 10a. The initiation of branching at the tip of an α lath, as seen experimentally, is also shown in Figure 10e. We have not attempted a statistical analysis of these effects in experiment since measurements of lath thickness and growth ledge height require that the plane of projection lies perpendicular to the habit plane, and because adjacent laths will affect the plane branching process in the manner shown below.

Figure 11 illustrates the underlying driving forces for the preferential growth of the ledges or steps into branches by superimposing, for various configurations of the a laths, the diffusional fluxes and isocontours of compositional profiles in the β phase at different locations ahead of the α/β interface. Figure 11a shows the effect of multiple steps. The starting a lath in this simulation

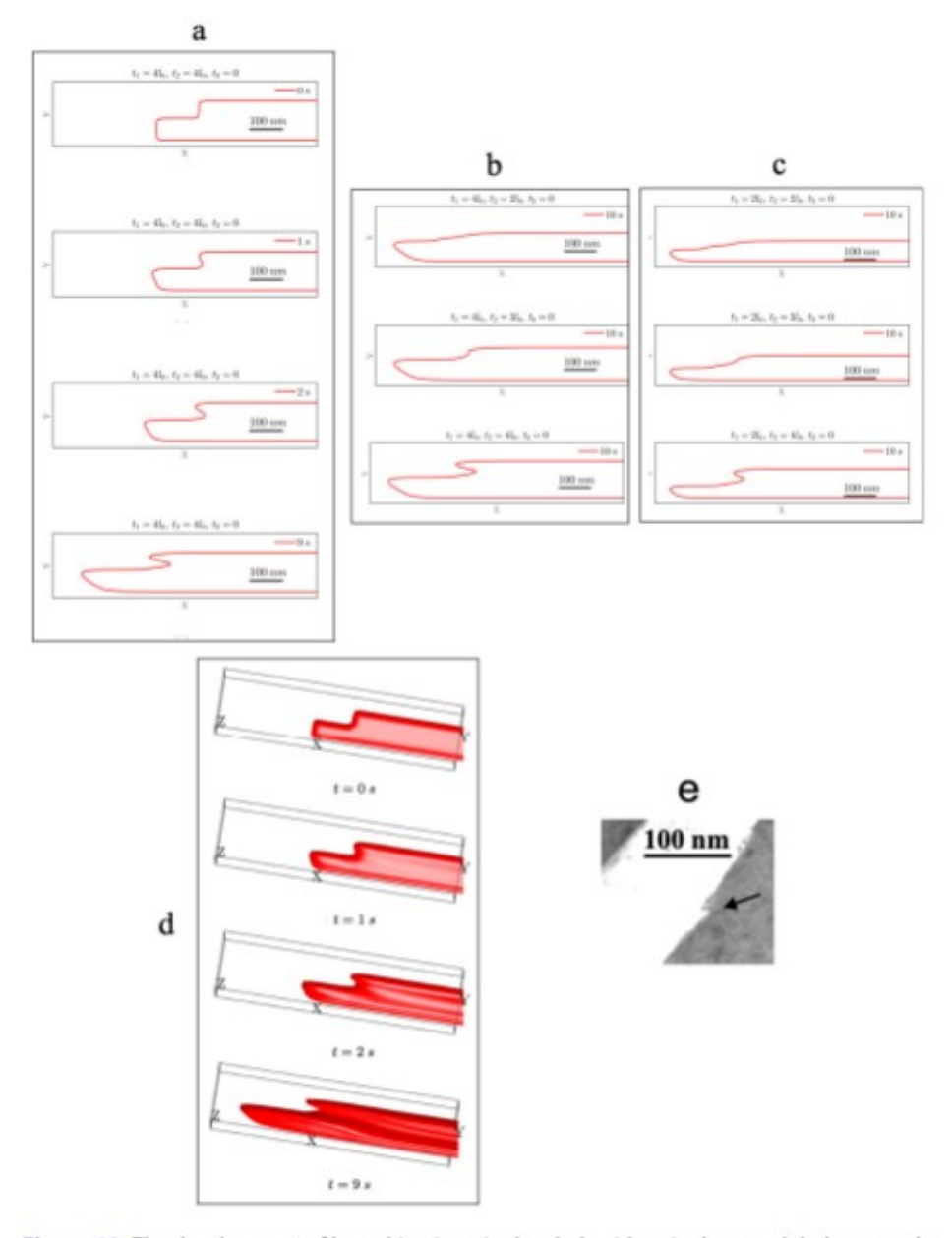


Figure 10. The development of branching in a single α lath with a single growth ledge near the lath tip. The starting configuration has $t_1 = 410$ nm, $t_2 = 410$ nm, $s_1 = 1010$ nm and $s_0 = 5010$ nm. The aging temperature is 800° C (a) the formation of branches at single step with the height equal to the base lath thickness. The image is a section through the 3d simulation in (d). (b) and (c) show the effect of step height and base lath thickness height for comparison. (e) The TEM image illustrates the initiation of the branching process from a ledge.

has 1 and 2 ledges for comparison. The magnitude of the diffusion fluxes of the α stabiliser Al (as an example) towards the α lath varies in different locations, with a higher flux at the step corners. Branches extend at equal rates from

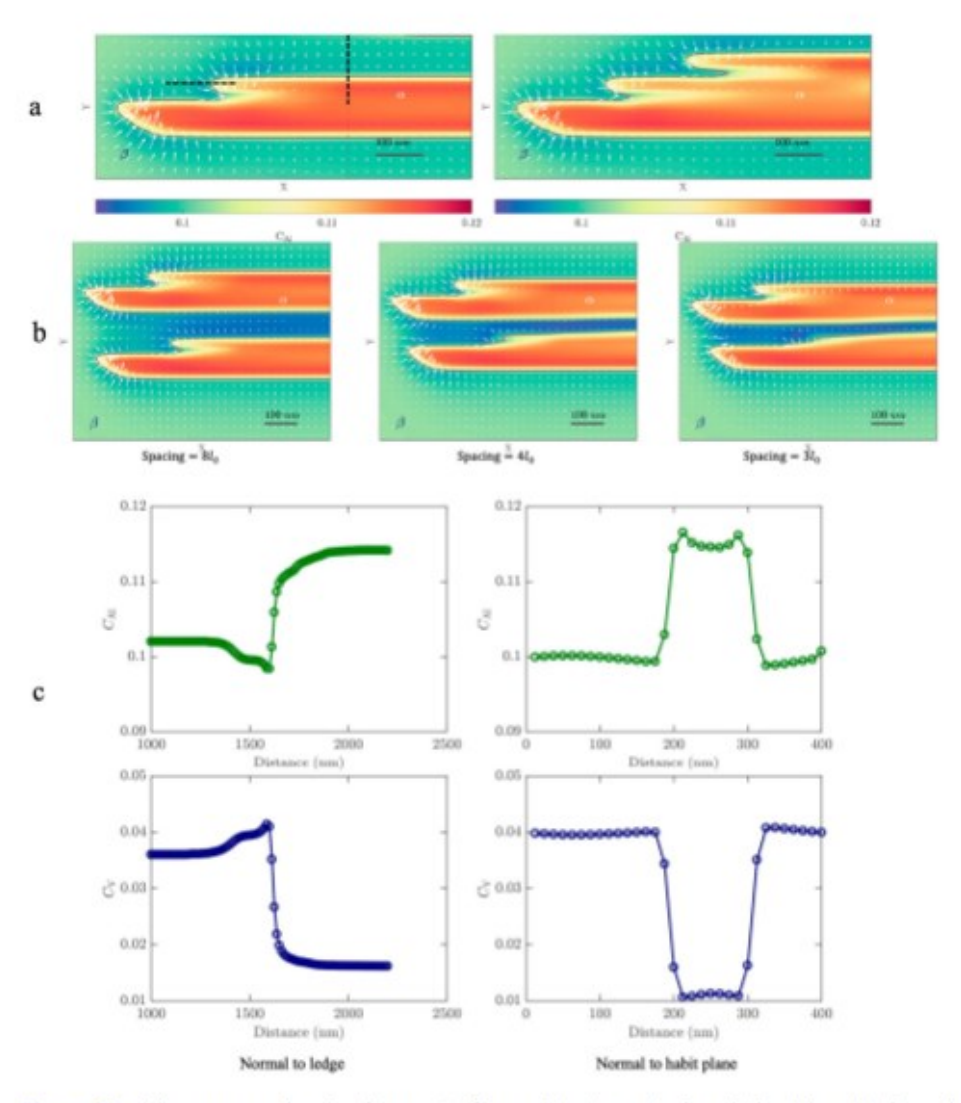


Figure 11. (a) compares the development of branching in a single α lath with a single and double growth ledges near the lath tip at 800°C. The starting configuration has $t_1 = t_2 = t_3$ =410 nm, s₁ = 1010 nm and the spacing between the tip and the step and between steps is $s_0 = 5010$ nm. (b) compares the effect of the spacing between two adjacent laths of the same crystallographic variant with a single ledge. The starting configuration in each lath is the same as in (a). White arrows denote diffusion flux (vectors) of the a stabiliser, Al. The length of the white vectors indicates the strength of the diffusion flux and the starting point of the vectors indicates the position at which the flux is shown. Isocontours of the Al concentration are superimposed (c) composition profiles for Al and V in the β phase perpendicular to the ledge tip and habit plane along the hatched lines in the left hand figure of (a). The step in the diffusion profile is discussed in the text.

multiple steps. Figure 11b assesses the effect of adjacent laths of the same crystallographic variant. The suppression of branching in the lower lath with decreasing lath spacing is apparent. Al is increasingly depleted between the two a laths as their spacing reduces, reducing the branching propensity for the growth ledges in the depleted zone. The diffusional flux is proportional to the concentration profiles in different locations, and Figure 11c illustrates the concentration profiles of Al and V in the β phase ahead of the tip of the ledge and perpendicular to the broad face, shown for the case of Figure 11a. The small step in the diffusion profiles of V and Al in β has probably arisen from the interaction of the diffusional field at the adjacent broad face with that associated with the step.

Figure 12 shows the effect of supersaturation and diffusivity on the development of branching in a single a lath -. The effect of ageing temperature (850°C, 800°C, 750°C) on branching in a single α lath is presented in Figure 12a-c. The lateral growth of the branches is faster at high temperatures. The degree of supersaturation increases while the diffusivity decreases with reduced ageing temperature for a given alloy composition. To separate these effects, branching in an alloy composition Ti-5.67Al-6.43V (wt.%) that lies on the same tie line at the ageing temperature of 800°C as Ti6Al4V is shown in Figure 12d. The tip radius decreases at reduced supersaturation. It is also seen that the branch tends to split from the main lath as it lengthens, driven possibly by the minimisation of elastic and interface energies. The experimental equivalent of the splitting process is shown in the 3d images in Figure 11e, where laths which appear separate in certain orientations are actually joined by narrow segments to the main lath. Data on lengthening rates of steps and the increase in volume fraction with time at different ageing temperatures is provided in the Figure S2 of the supplementary information.

4. Discussion

This study focuses on a systematic exploration of the β to α transformation in composition-temperature space using the Ti-Mo system as a model system. The results indicate that the growth of α precipitates occurs through multiple branching from the original laths in an extended region of composition and temperature space. These fine scale microstructural features during the β to α transformation have been shown in images in extensive earlier literature over decades. Branching has also been demonstrated in 3d representations of α growing from grain boundaries [22] and in fully transformed structures of the Ti6Al4V alloy [23]. Similar structures have been attributed to the presence of prior ω phase [24]. Our high throughput study enabled us to trace these branched structures from early stages in their formation to fully evolved α distributions, as shown in Figures 3–5.

Several features of such multiply branched structures should be pointed out:

(a) The extent of branching depends on the presence of adjacent α laths. Thus, the branching is easily observed at ageing temperatures and compositions with a relatively low volume fraction α (Figures 4,5), presumably

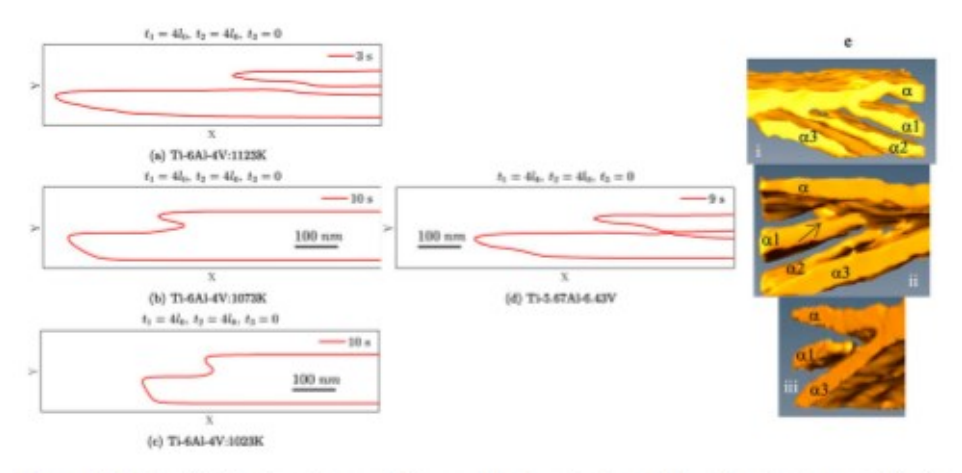


Figure 12. (a) to (c) The development of branching in a single α lath with a single growth ledge near the lath tip at different temperatures (850°C, 800°C and 750°C). The starting configuration has $t_1 = 410$ nm, $t_2 = 410$ nm, $s_1 = 1010$ nm and $s_0 = 5010$ nm as in earlier figures. In (d) the alloy composition in the β matrix is Ti-5.67Al-6.43V (wt.%) which lies in the same tie line as Ti-6Al-4V (wt.%) and the supersaturation is increased compared to Ti6Al4V since the α composition remains the same (e) a 3d image of a branched α lath: In (i) 3 branches α 1, α 2 and α 3 are emerging from of the main lath. α 3 appears as a separate lath not joined to the main lath. The image in (ii) is rotated by an approximately vertical axis by about 180° and further rotated in (iii). The branch α 1 is joined to the main branch by a narrow strip seen in (ii) marked by an arrow and appears completely separate in (iii) while the branch α 3 is now seen as joined to the main lath in (iii). The branch α 2 is not visible in (iii).

when diffusion fields from adjacent α laths do not overlap. Nevertheless, careful examination shows that branching or forking of the α laths is still observed to a limited extent even at high volume fractions, as seen in Figure 5a and c.

- (b) Branching or forking can occur from α sideplates originating from grain boundary α allotriomorphs (Figures 5a, 9b).
- (c) As a consequence of sectioning, the branched α structure can appear as groups of discrete α laths belonging to the same crystallographic variant, as shown in the 3D studies of Figure 6 and the TEM characterisation in Figure 8. Branched, intragranular α can therefore appear to form colony structures (Figure 4, Ti-3Mo and Figure 6c) that are usually associated with α sideplates that emerge from grain boundary α (Figure 4, Ti-1.5Mo). However, intragranular α bundles typically form in groups of 3 with a common [1120]α // [111]β direction (Figure 6), unlike α sideplates whose orientation is determined by the orientation of the grain boundary α from which they originate.
- (d) A careful orientation analysis with high resolution EBSD indicates that misorientation within such branched structures are on an average about 0.5°, without the presence of subgrains either within laths or where the branched structures are seen to join the main lath (Figure 7).

- (e) While such branching does not lead to a change in orientation relationship within the error of measurement, habit planes and growth directions scatter about a mean (Figure 8).
- (f) The phenomenon is not restricted to the Ti-Mo system but encompasses compositions with alloying elements commonly used in commercial titanium alloys (Figure 9).

Menon and Aaronson [8] and Aaronson et al. [25] analysed and attributed the formation of such branched structures to sympathetic nucleation based on the presence of subgrain boundaries in a plates, which they attributed to the interfaces created by such nuclei. The 3 types of sympathetic nucleation considered by them are edge to edge, edge to face and face to face. The morphology of the structures described in Figures 4-6 and 8 cannot possibly arise from edge-to-edge sympathetic nucleation, which leads to extended laths separated by subgrain boundaries perpendicular to the lengthening direction (see Figure 2a and b of [8]). The simplest explanation for the presence of such subgrains, that they could have arisen due to prior misorientations in the β phase, seems to have been ignored. The examples offered of edge to face nucleation in Figure 4 of [8] leads to the variant rotated 60° about a common $[11\bar{2}0]_{\alpha}$ axis (see Figure 4 of our paper and [20, 21]), which is again not the subject matter of discussion here. The example given by Menon and Aaronson of face-to-face sympathetic nucleation leads to a non-Burgers α, which has since been shown to be an artefact of thin foil preparation [26]. The closest case of sympathetic nucleation that can describe the branched structures observed by us would be described as an edge to face nucleation of the same crystallographic variant, requiring a high angle α/α boundary to have lower energy than a low energy α/β boundary.

Menon and Aaronson [8] specifically excluded the possibility of branching for the α/β case on the grounds that only a single low energy habit plane would be possible for such solid-state precipitation involving a single variant with the BOR. However, they did not take cognisance of the possibility that growth of instabilities balances diffusional, capillarity and elasticity effects as in solidification and solid-state dendritic branching. Our results clearly show that the lath bundles with branches are all in the same crystallographic orientation and yet contain habit planes that scatter about a mean. These branched a laths bear a close resemblance to solid-state dendritic structures that have been observed in the past (see [27-31] for more recent references). Shewmon [32] appears to have been the first to point out that dendritic morphologies would naturally evolve if precipitate growth were controlled by long-range diffusion alone. As indicated by Mullins and Sekerka [33] in their analysis of infinitesimal perturbations at the liquid/solid interface, the amplification of a protrusion is opposed by other factors such as anisotropy in surface and elastic energy. Phase field simulations have been applied in at least one instance



to examine the effects of elastic and surface energy anisotropies on solid-state dendrite evolution [31].

In the current study, we have therefore re-examined the possibility of branching of the a phase with phase field simulations. We have not analysed a Mullins-Sekerka instability itself but have introduced a pre-existing perturbation in the form of steps or growth ledges at the broad faces of the α/β interfaces as seen experimentally in Figure 3. The ledge density increases towards the tips of the α laths, as seen in Figure 3a. We examine the evolution of these steps with time under different conditions. Since the phenomenon appears to be common to various titanium compositions, we have used the reliable thermodynamic and kinetic databases available for Ti6Al4V in our simulations. The simulations demonstrate that branching can occur if steps are present on the habit planes of α laths due to the thickening of α phase by the ledge mechanism. We show that (a) a critical step height exists for branching to occur (Figure 10), although this feature has not been demonstrated experimentally (b) that branching can occur from multiple steps leading to continuous branching originating from a single lath, as seen in Figure 11a and experimentally in Figures 4-6 and Figure 8. The effect of overlapping diffusion fields arising from increasing a volume fraction has been assessed in the phase field simulations in Figure 11b and of supersaturation and diffusivity in Figure 12. These effects may be compared with experimental results that show the combined effect of transformation temperature and composition on these factors. Substantially increased branching is observed for increasing Mo content at the same transformation temperature (Figure 4) and with increasing transformation temperatures for the same Mo composition (compare, for instance, Figure 5b and c). The phase field simulations thus reproduce the general features of the experimental results. It must be pointed out that 3-dimensional and crystallographic effects make a statistical, quantitative assessment of these features a formidable challenge.

To understand the branching phenomenon, the atomic flux of Al (a stabiliser), $J_{Al}(X)$, related to the supersaturation in the β matrix is analysed, and the results are presented in Figure 11. We have chosen to show this for the species showing a slower interdiffusion rate, although more complex analysis for multicomponent diffusion is also available [34]. The flux vectors are visualised as white arrows and the sizes of the arrows are proportional to the magnitude of the fluxes. It is found that the magnitude of diffusion flux of Al towards the α lath varies in different locations and is larger at the tips of the growing instabilities, as might be expected from a consideration of the diffusion profiles shown in Figure 11c. Experimentally, however, a deviation from the habit plane is also observed as in Figure 8a, and the simulation carried out does not capture this feature. There is clearly a driving force for the branches to grow away from reduced supersaturation at that segment of the broad face which is just adjacent to the branch tip. It is possible that this is not observed in the simulation because the model lacks inbuilt mechanisms that would allow this process to occur with the least interface energy penalty at the habit plane, such as changes in structural ledge spacing [16] or growth ledge spacing. We also note that the time scale of phase field simulation is quite small but does demonstrate the inherent instability of the growth ledges.

The branched structures are also unstable, as shown by the splitting of the branched segments into individual plates in both simulation and experiment in Figure 12. Figure 13a shows the variation of growth rate (in our limited simulations) with the solutal Péclet number, RV/2D where R is the tip radius, V the growth velocity and D the effective diffusivity. The trend is similar to that observed during the growth of dendrites during solidification, as can be inferred from [35,36] with [34,37] as specific examples. However, the steady state tip radius increases with supersaturation, and this is the inverse of that expected during solidification [35, 36]. We suggest that this behaviour arises from a synergistic effect of significant anisotropy in interface energy and elastic energy effects. A decreased supersaturation is expected to result in a lower tip curvature if interface energy is isotropic. On the other hand, the tip will attempt to minimise the surface orientations associated with higher surface energies in the presence of a significant anisotropy [35]. In addition, elastic energy effects will assume increased dominance at lower supersaturations leading to a sharpening of the tip. We have indirectly explored these effects on tip curvature by changing the surface energy ratios while maintaining a constant elastic energy contribution and changing the elastic energy contribution while maintaining constant surface energy ratios. The results are provided in supplementary Figure S2. As this figure shows, a decrease in elastic energy contribution blunts the tip as does a reduction in surface energy anisotropy. We note that the shape of the tip is not a needle as in dendrite tips associated with solidification but resembles a plate with curved ends (Figure 10). A detailed analysis of tip radius selection is beyond the scope of the paper.

It is of some interest to consider whether sideplate formation from grain boundary α arises from a similar phenomenon of enhanced diffusion at corners of steps on grain boundary α or from a more general Mullins-Sekerka instability. We also note that though we have modelled branching from growth ledges accumulated at the tips of alpha laths, such branching would also be possible from growth ledges anywhere on the broad face provided that the ledge height was large enough to initiate the instability.

In summary, we have demonstrated that extensive branching of α laths is a ubiquitous phenomenon occurring over a broad range of composition and temperature space during the β to α transformation in titanium alloys. Although such structures have been attributed earlier to sympathetic nucleation, a solid-state dendritic growth phenomenon in the presence of growth ledges provides a viable alternative explanation for these morphologies. We

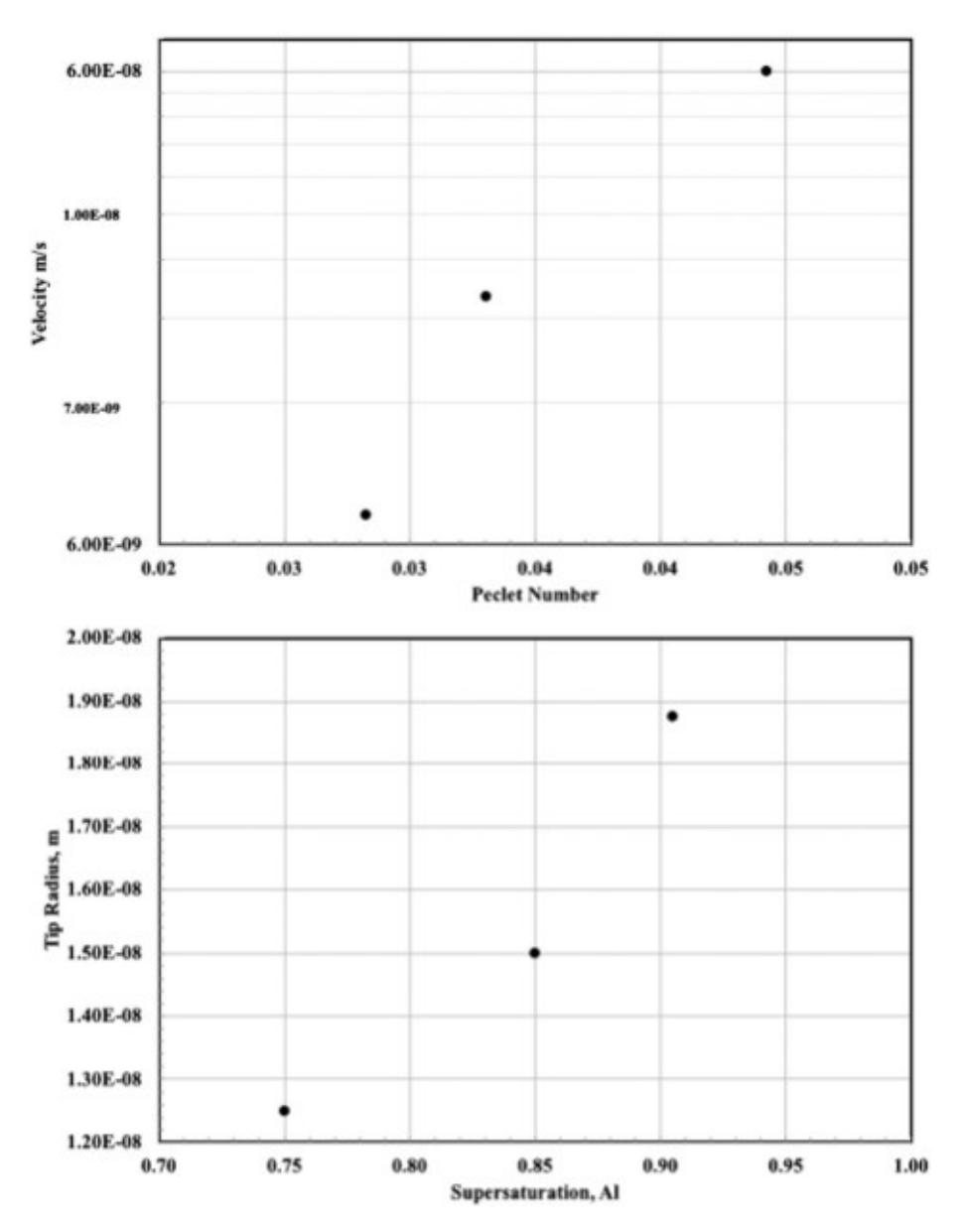


Figure 13. (a) steady state growth rate plotted against the Peclet number and (b) the tip radius plotted against the Al supersaturation for different aging temperatures.

note that regions of parallelly oriented intragranular a laths arising from branching affect mechanical behaviour, providing extended mean free paths from slip since they effectively act as 'single crystal' regions arising from easy slip transfer between similarly oriented a and \$\beta\$ [38]. Such regions are also at the origin of macrozones of similarly oriented a that form during thermomechanical processing with consequences for dwell fatigue behaviour of titanium alloys [39].



5. Conclusion

It has been demonstrated that the β to α transformation is associated with significant branching of α laths during growth. Multiply branched α laths can form over a large region of composition and temperature space but are less obvious (although present) at compositions and temperatures where the volume fraction of α is high such that the diffusion fields from adjacent α laths start to overlap. Branching of intragranular a laths leads to the bundles of parallel a laths of the same variant, with a resulting colony like appearance. Such multiply branched a laths cluster in groups of 3 bundles that share a common [1120] / [111] direction arising from the Burgers orientation relationship. The branching process has been simulated using the phase field method that satisfactorily explains that branching initiates from ledges on the habit plane of a laths.

Acknowledgements

We - acknowledge support from NSF-DMR-1905844 and NSF-DMREF-1435611 grants. The authors also gratefully acknowledge the use of equipment in Materials Research Facility (MRF) at the University of North Texas. One of the authors, DB, acknowledges the JC Bose Fellowship of the Department of Science and Technology, India and the Raja Ramanna Fellowship. A substantial portion of this work was carried during the visits of DB to the University of North Texas. Part of the work (R. Shi) was supported Laboratory Directed Research and Development programme at LLNL under the project tracking code 18-SI-003 and 20-SI-004. This phase field simulations were also supported in part by the allocation of computing time from the Ohio Supercomputer Center. The authors acknowledge the support of Tushar Borkar, Soumya Nag and Pavani Kami at the University of North Texas and Shanoob Balachandran at the Indian Institute of Science in various aspects of this study. Discussions with Abhik Choudhury of the Materials Engineering Department of the Indian Institute of Science are gratefully acknowledged.

Disclosure statement

No potential conflict of interest was reported by the author(s).

Funding

This work has been supported by the ISES contract awarded to the University of North Texas by the U.S. Air Force Research Laboratory, AFRL contract number FA8650-08-C-5226; Division of Materials Research; Lawrence Livermore National Laboratory, USA.

ORCID

Deep Choudhuri Dhttp://orcid.org/0000-0002-5007-4249 Yunzhi Wang http://orcid.org/0000-0003-3247-297X Dipankar Banerjee Dhttp://orcid.org/0000-0002-9670-4824



References

- [1] D. Banerjee and J.C. Williams, Perspectives on titanium science and technology. Acta Mater. 61 (2013), pp. 844-879.
- [2] G. Lutjering and J.C. Williams, Titanium, 2nd ed., Springer, Heidelberg, 2007.
- S. Nag, R. Banerjee, R. Srinivasan, J.Y. Hwang, M. Harper and H.L. Fraser, ω-Assisted nucleation and growth of α precipitates in the Ti-5Al-5Mo-5V-3Cr-0.5Fe β titanium alloy. Acta Mater. 57 (2009), pp. 2136-2147.
- [4] D.J. DeLazaro, M. Hansen, R.E. Riley and W. Rostoker, Time-temperature-transformation characteristics of titanium-molybdenum alloys. Trans. AIME 194 (1952), pp. 265-269.
- [5] T. Furuhara, T. Makino, Y. Idei, H. Ishigaki, A. Takada and T. Maki, Morphology and crystallography of α precipitates in β Ti-Mo binary alloys. Mater. Trans. JIM 39 (1998), pp. 31-39.
- [6] D. Choudhuri, T. Borkar, R. Banerjee and D. Banerjee, Mapping the decomposition of β to α in composition and temperature space in titanium alloys, in Proceedings of the 13th World Conference on Titanium, J.E. Allison, S. Ankem, R. Boyer, J. Christodoulou, H.L. Fraser, M.A. Imam, Y. Kosaka, H.J. Rack, A. Chatterjee, A. Woodfield, ed., TMS (The Minerals, Metals & Materials Society), Hoboken, 2016, pp. 515-509.
- [7] M. Unnikrishnan, E.S.K. Menon and S. Banerjee, Kinetics of α precipitation in Ti-6 wt % Cr and Ti-11wt % Mo. J. Mater. Sci 13 (1978), pp. 1401-1410.
- [8] E.S.K. Menon and H.I. Aaronson, Morphology, crystallography and kinetics of sympathetic nucleation. Acta Metall. 35 (1987), pp. 549-563.
- [9] J. I. Goldstein, Principles of thin film x-ray microanalysis, in Introduction to Analytical Electron Microscopy, J.J. Hren, J.I. Goldstein, D.C. Joy, ed., Springer, New York, 1979. pp. 83-120.
- [10] A. Kashiwar. 3d microstructural characterisation in some alloys using serial sectioning techniques, Masters Thesis, Indian Institute of Science, Bangalore, India, 2014.
- [11] Q. Chen, N. Ma, K. Wu and Y. Wang, Quantitative phase field modelling of diffusioncontrolled precipitate growth and dissolution in Ti-Al-V. Scripta Mater. 50 (2004), pp. 471-476.
- [12] R. Shi, N. Ma and Y. Wang, Predicting equilibrium shape of precipitates as function of coherency state. Acta Mater. 60 (2012), pp. 4172-4184.
- [13] R. Shi and Y. Wang, Variant selection during alpha precipitation in Ti-6Al-4V under the influence of local stress - a simulation study. Acta Mater. 61 (2013), pp. 6006-6024.
- [14] D. Qiu, R. Shi, D. Zhang, W. Lu and Y. Wang, Variant selection by dislocations during alpha precipitation in alpha/beta titanium alloys. Acta Mater. 88 (2015), pp. 218-231.
- [15] R. Shi, N. Zhou, S. Niezgoda and Y. Wang, Microstructure and transformation texture evolution during alpha precipitation in polycrystalline alpha/beta titanium alloys - a simulation study. Acta Mater. 94 (2015), pp. 224-243.
- [16] T. Furuhara, J.M. Howe and H.I. Aaronson, Interphase boundary structures of intragranular proeutectoid a plates in a hypoeutectoid Ti-Cr alloy. Acta Metall. Mater. 39 (1991), pp. 2873-2886.
- [17] T. Furuhara, T. Ogawa and T. Maki, Atomic structure of interphase boundary of a precipitate plate in a Ti-Cr alloy. Phil. Mag. Lett. 72 (1995), pp. 175-183.
- [18] F. Ye, W.-Z. Zhang and D. Qiu, A TEM study of the habit plane structure of intragranular proeutectoid a precipitates in a Ti-7.26 wt%Cr alloy. Acta Mater. 52 (2004), pp. 2449-2460.
- [19] Y. Zheng, R.E.A. Williams, G.B. Viswanathan, W.A.T. Clark and H.L. Fraser, Determination of the structure of α - β interfaces in metastable β -Ti alloys. Acta Mater. 150 (2018), pp. 25-39.



- [20] S. Balachandran, A. Kashiwar, A. Choudhury, D. Banerjee, R. Shi and Y. Wang, On variant distribution and coarsening behaviour of the α phase in a metastable β titanium alloy. Acta Mater. 106 (2016), pp. 374-387.
- [21] N. Miyano, T. Norimura, T. Inaba and K. Ameyama, Reasons for formation of triangular precipitates in Ti-15V-3Cr-3Sn-3Al β titanium alloy. Mater. Trans. JIM 47 (2006), pp. 341-347.
- [22] H. Sharma, S.M.C. van Boheman, R.H. Petrov and J. Sietsma, Three-dimensional analysis of microstructures in titanium. Acta Mater. 58 (2010), pp. 2399-2407.
- [23] R. DeMott, P. Collins, C. Kong, X. Liao, S. Ringer and S. Primig, 3D electron backscatter diffraction study of α lath morphology in additively manufactured Ti-6Al-4V. Ultramicroscopy 218 (2020), p. 113073.
- [24] N.G. Jones, R.J. Dashwood, M. Jackson and D. Dye, Development of chevron-shaped a precipitates in Ti-5Al-5Mo-5V-3Cr. Scripta Mater. 60 (2009), pp. 571-573.
- [25] H.I. Aaronson, G. Spanos, R.A. Masamura, R.G. Vardiman, D.W. Moon, E.S.K. Menon and M.G. Hall, Sympathetic nucleation: an overview. Mater. Sci. Eng. B 32 (1995), pp. 107-123.
- [26] D. Banerjee, C.G. Sheldon, B. Ralph and J.C. Williams, A resolution of the interface phase problem in titanium alloys. Acta Metall. 36 (1988), pp. 125-141.
- [27] S.R. Summerfelt and C.B. Carter, Morphology of NiFe₂O₄ precipitation in NiO. Acta Metall. Mater. 40 (1992), pp. 1051-1067.
- [28] S.W. Husain, M.S. Ahmed and I. Qamar, Dendritic morphology observed in the solidstate precipitation in binary alloys. Metall. Mater. Trans. A 30A (1999), pp. 1529-1534.
- [29] A.N. Khan, I. Salam and A. Tauqir, Formation of solid-state dendrites in an alloy steel. Surf. Coat. Technol. 179 (2004), pp. 33-38.
- [30] Y.S. Yoo, Morphological instability of spherical y' precipitates in a nickel base superalloy. Scripta Mater. 53 (2005), pp. 81-85.
- [31] M. Greenwood, J.J. Hoyt and N. Provatas, Competition between surface energy and elastic anisotropies in the growth of coherent solid-state dendrites. Acta Mater. 57 (2009), pp. 2613-2623.
- [32] P.G. Shewmon, Interfacial stability in solid-solid transformations. Trans. TMS-AIME 233 (1965), pp. 736-748.
- [33] W.W. Mullins and R.F. Sekerka, Morphological stability of a particle growing by diffusion or heat flow. J. Appl. Phys. 34 (1963), pp. 323-329.
- [34] A. Lahiri and A. Choudhury, Dendrite tip selection during isothermal free growth in multi-component alloys: marginal stability theories and insights from phase-field simulations. Comput. Mater. Sci. 158 (2019), pp. 209-218.
- [35] W. Kurz and D.J. Fisher, Fundamentals of Solidification, Trans Tech Publications, Switzerland, 1998.
- [36] J.A. Dantzig and M. Rappaz, Solidification, 2nd ed., EPFL Press, Lausanne, 2016.
- [37] B. Nestler, D. Danilov and P. Galenko, Crystal growth of pure substances: phase-field simulations in comparison with analytical and experimental results. J. Computational Phys. 207 (2005), pp. 221-239.
- [38] S. Hemery, P. Villechaise and D. Banerjee, Microplasticity at room temperature in α/β titanium alloys. Metall. Mater Trans. A 51 (2020), pp. 4931-4969.
- [39] N. Gey, P. Bocher, E. Uta, L. Germain and M. Humbert, Texture and microtexture variations in a near-α titanium forged disk of bimodal microstructure. Acta Mater. 60 (2012), pp. 2647-2655.